Elastic and thermodynamic properties of the major clinker phases of Portland cement: Insights from first principles calculations

Ngoc Lan Mai [a], Nguyen-Hieu Hoang [b], Ha T. Do [a], Monika Pilz [b], Thuat T. Trinh [c,*]

[a] *Faculty of Applied Sciences, Ton Duc Thang University, Ho Chi Minh City, Viet Nam*
[b] *Department of Materials and Nanotechnology, SINTEF Industry, Norway*
[c] *Department of Civil and Environmental Engineering, Norwegian University of Science and Technology – NTNU, Norway*

HIGHLIGHTS

- A systematic DFT calculations for cement clinker phases are presented.
- Spin-polarized treatment is crucial for ferrite structure.
- The calculated elastic, thermodynamic properties agree well with experimental data.
- More insight into the atomic charge is provided.

ARTICLE INFO

ABSTRACT

Portland based cement is one of the most popular materials used in the civil and construction applications. Reliable computational methods to provide an insight into the underlying mechanics of the major phases of this material are of great interest for cement design. The present work investigated the performance of density functional theory (DFT) calculations using the PBE-D2 method to predict the mechanical, thermodynamic properties of four major phases namely Alite C_3S, Belite C_2S, tricalcium aluminate C_3A and tetracalcium aluminoferrite C_4AF. The calculated elastic properties were in a good agreement with available experimental data. In addition, a deeper insight into the electron density of state, spin-polarization, atomic charge, as well as free energy and entropy properties were also presented. Further development is necessary to improve the established DFT models for predicting the mechanical properties of the ferrite phase of Portland clinker.

© 2021 The Author(s). Published by Elsevier Ltd. This is an open access article under the CC BY license (http://creativecommons.org/licenses/by/4.0/).

1. Introduction

Portland cement remains by far the most common and prominent type of cement in general use around the world today. It is not only widely used in the civil and construction application as binding material but also in cementing O&G and geothermal wells. This cement was invented in the early 1800s, as a product of extreme-heating limestone ($CaCO_3$) with other materials (e.g. clays) in a process called calcination. The resulting hard substance, called 'clinker', is then ground into a small powder to produce Portland cement. Portland cement clinker contains four principal minerals, namely Alite C_3S, Belite (C_2S), tricalcium aluminate C_3A and tetracalcium aluminoferrite C_4AF. Alite C_3S represents the most crucial phase of Portland cement clinker, constituting of approximately 65% of the total clinker weight. This phase is responsible for short-term properties and early strength of the cement paste. The second important phase is Belite (C_2S), constituting of about 15% of the total clinker weight, has most influence on long-term cement properties. C_3A and C_4AF are of secondary importance in comparison to C_3S and C_2S on cement properties[1]. In addition to these chemical compounds, some other resulting phases are also formed in the clinker phase. They are results from existing less-important oxides in the primary materials. These phases, however, do not play significant roles on the final mechanical properties of cement paste. Understanding mechanical properties of the four principal Portland cement phases is crucial to progressively improve the production of cement hydrates and enhance the subsequent performance of cemented structures.

Getting an insight into microstructure and properties of these constituents at the nanoscale level is fundamentally important for a deeper understanding of cement materials. However, given the experimental limitations, very few data concerning mechanical features of Portland clinker phases can be found in the open liter-

---

ature [2,3]. In the work of Velez et al. [2], the elastic behaviour of the main clinker phases were investigated both at the microscopic scale by nanoindentation and at the macroscopic scale by the resonance frequencies technique. At the microscopic scale, the elastic Young's moduli of the four main phases were reported to be between 125 GPa and 145 GPa. The elastic moduli were found to be a function of the bulk porosity of the samples. By extrapolating to zero porosity, the macroscopic scale results were shown to be in a good agreement with the results obtained at the microscopic scale by nanoindentation. More recently, Sebastiani et al. [4] have adopted a more advanced technique of high resolution and high-speed nanoindentation to probe that the elastic modulus of the hydrated C-S-H phase is independent of hydration time. Another study was conducted by Boumiz et al. [3] in which the transmission of ultrasonic wave method was employed to calculate the C_3S elastic modulus. However, there is still a lack of a systematic understanding of the mechanical properties of Portland clinker, and yet many properties and interactions of cement pastes are remained unexplored due to the cost required for extensive testing or due to the current limitations of experimental techniques.

Advanced modelling and simulations methods have demonstrated a great potential to expand the fundamental knowledge of cement phases, thereby identifying the key parameters and reducing the tests quantity necessary for material development. Among the available modelling techniques, molecular dynamics using force field methods is very effective to simulate different compounds and relate those to the mechanical properties of materials. These approaches have recently been used in various structures and scientific works. In several studies, Manzano et al. [5–7] have used classical force field atomistic methods to investigate the elastic and reactivity properties of C_3S, C_2S and C_3A. In their recent examination, the authors even used the combination of classical and quantum mechanical simulation methods to study the detailed physicochemical changes of the clinker phases C_3S and C_2S when guest ions are incorporated into their structure [8]. In another work performed by Mishra et al. [9,10], molecular dynamics simulation was additionally used to estimate properties of C_3S. Although molecular dynamics seems to be an effective tool to understand the microstructure behaviour of cement phases, the choice of force field methods has a great impact on the resulting mechanical properties, as recently demonstrated by the work of Tavakoli et al. [11]. More recently, Mishra et al. [12] reviewed the performance of several force fields such as CSH-FF [13], IFF [14] and ReaxFF [15] to reproduce physical and chemical properties of C_3S and other cementitious systems and discussed the strength and limitations of each force field. Application of the FF to calculate cleavage energy, hydration energy of the cement phases was also reported [12,16]. However, there is limited force field method that can capture the mechanics of the ferrite phase of Portland clinker.

Besides molecular dynamics based force field methods, ab initio atomistic simulations based on the density functional theory (DFT) have gained much recognition among the research community in a wide application range like physics, chemistry biology, mineralogy, engineering and other related areas. The first principles methods, or ab initio methods, are derived directly from theoretical principles and do not fit any empirical parameters during the calculation. There are different levels of approximation depending on the treatment of electronic correlation and the influence of relativistic effects. The properties of the system can be calculated with functions of a spatially dependent electron density using this theory. The Perdew-Burke-Ernzerhof [17] (PBE) method is one of the most common functions in solid state physics calculations. DFT simulation of nanoscale crystal structure could essential information of the interested material such as lattice parameters, total energy, mechanical properties, thermodynamic properties. More details

can be found in some excellent reviews of computational application in material sciences elsewhere [18–20]. However, given the large unit cell and the complexity of Portland cement phases' structure, very few simulations based on purely DFT were performed to determine the materials properties. Additionally, the reactions in cement material are often so complex that they could not be completely represented by either force fields or by DFT. For example, the reactions involve several length scales, complex ionic electrolytes, and time scales that are beyond any DFT or FF model's capabilities. Force fields were used to characterize electrolyte interfaces and to locally deduce critical correlations with surface reactivity [21,22]. Many research works have attempted to employ the combination of force field based simulations and DFT simulations to gain atomic level insight into the structure and property of cement phases and its hydration products [5,23–26]. Recently, Laanaiya et al. [27] performed purely DFT calculations to obtain insight into structural, electronic and mechanical properties of C_3S. Their results in terms of elastic properties were in an excellent agreement with C_3S test results documented by Velez et al. [2]. Although only the Alite phase C_3S was investigated [27], their work has shown the great potential of ab initio atomistic calculations for expanding the fundamental understanding of cement materials.

The main objective of the present paper is to evaluate the capability to predict the thermal–mechanical properties of all the four principal phases of Portland clinkers using only one DFT computation method. To this end, DFT based models of the four materials were established and optimized. Simulations of the four clinker phases were performed using the so-called PBE-D2 method and numerical results were compared with experimental data available in the open literature. The established models were then used to provide a deeper understanding of electronic and thermodynamic properties of the four investigated materials. The paper is organized as follows: Computational methods and models are presented in Section 2. Section 3 discussed the obtained results. Finally, concluding remarks are summarized in Section 4.

2. Models and methods

The initial configurations of all clinker structures were obtained from experimental data and then the unit cell parameters and atomic positions were optimized with DFT method. The chemical composition in the simulation cells was $Ca_8Si_4O_{16}$, $Ca_{54}Si_{18}O_{90}$, $Ca_{72}Al_{48}O_{144}$, $Ca_8Al_4Fe_4O_{20}$ for C_2S, C_3S, C_3A, C_4AF, respectively. We typically used pseudo-potentials from the GBRV pseudo-potentials library [28] and the generalized gradient approximation (GGA) in the Perdew-Burke-Ernzerhof method [17] (PBE) as implemented in the Quantum Espresso simulation package [29]. The electron valence was taken as 10e, 4e, 6e, 3e, 16e for Ca, Si, O, Al and Fe atoms, respectively. After thorough convergence tests, the kinetic energy and charge density cutoffs of 60 Ry and 700 Ry were taken, respectively. Based on the size of the unit cell and total atoms of the simulation cell, **k**-points mesh was taken as (3 3 3) for C_2S, (4 2 4) for C_4AF, while **k**-points of (1 1 1) was selected for C_3S and C_3A due to their large number of atoms (162 atoms for C_3S and 264 atoms for C_3A). The structures of four clinker phases were plotted in Fig. 1 with VESTA package [30]. The electronic properties of the materials were investigated with the calculation of density of state (DOS) and the partial charge calculations. The Löwdin approach [31] was selected to determine the atomic charge and to compare with other methods. Some of the DOS calculations were performed with Quantum Espresso module in SCM-ADF package [32]. The PBE functional is one of the most common DFT methods in solid state calculation and was previously applied to study the properties of C_3S and C_3A phases [5,27]. However, the effect of Van-der-Waals (VdW) correction was not considered.
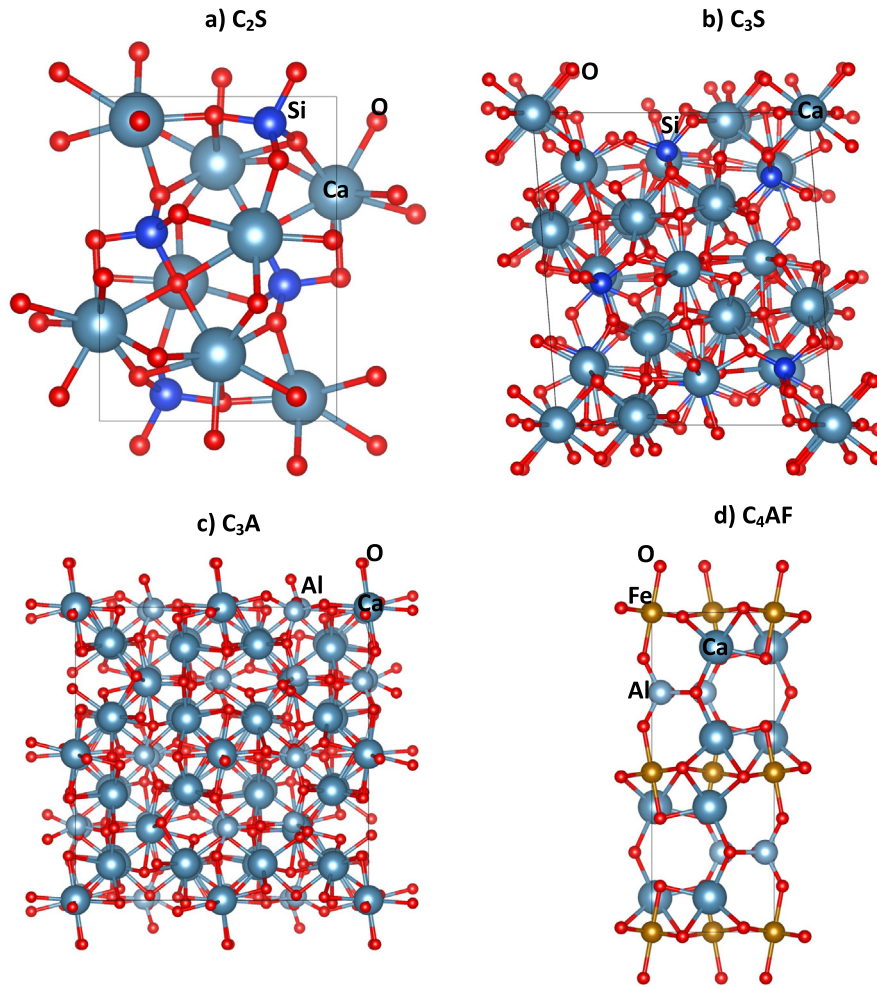
Fig. 1. Optimized crystal structure of the major clinker phase of Portland cement from DFT-PBE-D2 calculation: C_2S (a), C_3S (b), C_3A (c), and C_4AF (d). See the text for more details.

Thus, in our work the VdW correction was added using Grimme 2D approach [33]. We denoted our method as DFT-PBE-D2. In addition, we have tested another DFT approach, i.e. the Local Density Approximation (DFT-LDA), only for the C_2S phase. The corresponding simulations results of C_2S shown in Section 3 depicted a better predictive performance of DFT-PBE-D2 method than that of DFT-LDA. Thus, DFT-PBE-D2 was used in the rest of the work. In the subsequent of this paper, the term DFT denotes the specific method DFT-PBE-D2 if not otherwise specified.

In order to evaluate the elastic properties of the clinker phases, we used the established method in the computational material outlined briefly here. The generalised Hooke's Law for a linear elastic material is written

$$\begin{bmatrix} \sigma_1 = \sigma_{xx} \\ \sigma_2 = \sigma_{yy} \\ \sigma_3 = \sigma_{zz} \\ \sigma_4 = \sigma_{yz} \\ \sigma_5 = \sigma_{xz} \\ \sigma_6 = \sigma_{xy} \end{bmatrix} = \begin{bmatrix} C_{11} & C_{12} & C_{13} & C_{14} & C_{15} & C_{16} \\ C_{21} & C_{22} & C_{23} & C_{24} & C_{25} & C_{26} \\ C_{31} & C_{32} & C_{33} & C_{34} & C_{35} & C_{36} \\ C_{41} & C_{42} & C_{43} & C_{44} & C_{45} & C_{46} \\ C_{51} & C_{52} & C_{53} & C_{54} & C_{55} & C_{56} \\ C_{61} & C_{62} & C_{63} & C_{64} & C_{65} & C_{66} \end{bmatrix} \begin{bmatrix} \varepsilon_1 = \varepsilon_{xx} \\ \varepsilon_2 = \varepsilon_{yy} \\ \varepsilon_3 = \varepsilon_{zz} \\ \varepsilon_4 = \varepsilon_{yz} \\ \varepsilon_5 = \varepsilon_{xz} \\ \varepsilon_6 = \varepsilon_{xy} \end{bmatrix} \quad (1)$$

This notation with only one subscript for the stress and strain, numbered from 1...6, is helpful as it allows the equations of anisotropic elasticity to be written in matrix form. The 36's C_{ij} are called

the stiffnesses. The matrix of stiffnesses is called the stiffness matrix. This matrix can be inverted so that the strains are given explicitly in terms of the stresses:

$$\begin{bmatrix} \varepsilon_1 \\ \varepsilon_2 \\ \varepsilon_3 \\ \varepsilon_4 \\ \varepsilon_5 \\ \varepsilon_6 \end{bmatrix} = \begin{bmatrix} S_{11} & S_{12} & S_{13} & S_{14} & S_{15} & S_{16} \\ & S_{22} & S_{23} & S_{24} & S_{25} & S_{26} \\ & & S_{33} & S_{34} & S_{35} & S_{36} \\ & & & S_{44} & S_{45} & S_{46} \\ & & & & S_{55} & S_{56} \\ & & & & & S_{66} \end{bmatrix} \begin{bmatrix} \sigma_1 \\ \sigma_2 \\ \sigma_3 \\ \sigma_4 \\ \sigma_5 \\ \sigma_6 \end{bmatrix} \quad (2)$$

The elastic constants C_{ij} and constituents of the compliance tensor S_{ij} were calculated using external package Thermo-pw [34]. From the calculated C_{ij} and S_{ij}, the polycrystalline corresponding bulk modulus K and shear modulus G are determined using the Voigt-Reuss-Hill (VRH) approximation, as shown in Eqs. (3) and (4). In these equations, the underscripts R and V denote Reuss and Voigt bounds, respectively.

$$K_R = \frac{1}{S_{11} + S_{22} + S_{33} + 2(S_{12} + S_{23} + S_{31})}$$
$$K_V = \frac{C_{11} + C_{22} + C_{33} + 2(C_{12} + C_{23} + C_{31})}{9} \quad (3)$$
$$K = \frac{K_R + K_V}{2}$$

$$G_R = \frac{15}{4(S_{11} + S_{22} + S_{33}) - 4(S_{12} + S_{23} + S_{31}) + 3(S_{44} + S_{55} + S_{66})}$$

$$G_V = \frac{C_{11} + C_{22} + C_{33} - (C_{12} + C_{23} + C_{31}) + 3(C_{44} + C_{55} + C_{66})}{15}$$

$$G = \frac{G_R + G_V}{2}$$

$$(4)$$

The Young's modulus, E, and Poisson's ratio, v, for an isotropic material can be then estimated by:

$$E = \frac{9KG}{3K + G}, \quad v = \frac{3K - 2G}{6K + 2G} \qquad (5)$$

The spacial dependence of mechanic properties was plotted using Elate package [35]. The thermodynamic properties such as Gibbs free energy, entropy and heat capacity were calculated with phonon calculation using the package Thermo-pw [34]. The implementation of thermal properties calculation was described the work of Palumbo et al. [36]. Due to a relative large unit cell, a **q**-points mesh of 2x2x2 was applied and was tested to yield a good convergence in phonon calculation.

3. Results and discussion

3.1. Lattice constants

The structures of these materials were optimized by DFT simulation and the results are presented in Table 1. The initial structure were typically taken from the experimental data. The optimization results show that the lattice vector from DFT results was within 1% of the expected value, while the angles are in excellent agreement with experimental data.

The DFT-LDA approach seems to slightly underestimates the lattice parameters of the C_2S phase. However, the obtain structure of C_2S is still in good agreement with experimental, see Table 1. The Van-der-Walls effect was also investigated for C_2S structure. No major effect of VdW correction on the predicted material's lattice parameters was found. All the constant lattices vary only within 1% of the desired values. The DFT-calculated lattice parameters for C_2S, C_3S, and C_3A are within 1% of the experimental ones. Among the classical force fields, IFF seems to provide a reasonable prediction for these parameters of all phases within 2% error.

For C_4AF structure, the geometry optimization was performed with and without spin-polarized calculation. Both anti-ferromagnetic and ferromagnetic configuration were investigated. The results show that the anti-ferromagnetic phase is more stable than both the ferromagnetic and the spin-unpolarized phases. This is consistent with other reports [37]. The most stable configuration for C_4AF contains two Fe atoms with the polarization of 3.7 μB and two Fe atom with -3.7 μB. The calculated magnetic moment of Fe atom is in good agreement with other theoretical work for ion oxides[37]. Thus, the total magnetic moment of C_4AF is zero. The lattice constant of the anti-ferromagnetic structure is in excellent agreement with experimental data for C_4AF (see Table 1). The calculation with unpolarized phases underestimated all crystal parameters, especially for the b-axis. Thus, it is of importance to account for the magnetic moment with Fe ion in the ferrite crystal.

3.2. Mechanical properties

In this section, the numerical elastic properties of the four clinker phases obtained from this work are compared with both the numerical results and the experimental results found in the litera-

Table 1

Optimized lattice parameter of the four major clinker phases of Porland cement. The values from classical force field calculations and experimental data were taken from literature for comparison.

Phases	Method	Latice parameters		
		a (Å)	b (Å)	c (Å)
C_2S	Exp. [38]	5.5	6.75	9.34
	DFT-LDA (this work)	5.42	6.6	9.09
	DFT-PBE-D2 (this work)	5.45	6.7	9.19
	COM. [11]	4.97	6.1	8.43
	COM.II [11]	5.27	6.46	8.93
	ClayFF. [11]	5.4	6.61	9.15
	Dreid. [11]	5.71	7	9.68
	Universal [11]	5.5	6.75	9.34
	CVFF. [11]	5.62	6.89	9.54
	INTERFACE[11]	5.6	6.87	9.51
C_3S	Exp. [39]	11.63	14.17	13.64
	DFT-PBE-D2 (this work)	11.51	14.11	13.52
	COM. [11]	10.16	12.4	11.95
	COM.II [11]	10.5	12.8	12.31
	Dreid. [11]	11.92	14.55	14.02
	Universal [11]	12.57	15.34	14.78
	CVFF. [11]	11.76	14.35	13.82
	INTERFACE [11]	12.13	14	12.98
C_3A	Exp. [40]	15.26	15.26	15.26
	DFT-PBE-D2 (this work)	15.13	15.13	15.13
	COM. [11]	16.79	16.79	16.79
	COM.II [11]	16.95	16.95	16.95
	ClayFF [11]	14.64	14.64	14.64
	Dreid. [11]	15.35	15.35	15.35
	Universal [11]	16.03	16.03	16.03
	CVFF. [11]	15.56	15.56	15.56
	INTERFACE [11]	15.26	15.26	15.26
C_4AF	Exp. [41]	5.58	14.6	5.37
	DFT-PBE-D2 (this work)	5.49	14.16	5.23
	DFT-PBE-D2 spin-polarized (this work)	5.55	14.63	5.32
	ClayFF [11]	5.44	14.23	5.24
	Dreid. [11]	5.33	13.94	5.13
	Universal [11]	5.64	14.73	5.42

ture. The experimental results by Velez et al. [2] reported a comprehensive and systematic research work to investigate the mechanical properties of all the four clinker phases. In their work, nanoindentation techniques were first used to provide insights into the elastic behaviour of the four materials at the microscopic scale. Assuming a Poisson's ratio of 0.3, the authors could derive the Young's moduli of the investigated materials, based on the obtained hardness measurement. At the microscopic scale, the elastic Young's moduli of the four main phases were estimated to be between 125 GPa and 145 GPa. The influence of the porosity on the elastic behaviour was also investigated in their work. The elastic modulus were found to be a decreased function of the increasing bulk porosity of the investigated materials. By extrapolating to zero porosity, the macroscopic scale modulus were obtained. The reported macro results were between 147 GPa and 160 GPa. These values are very consistent with those on the microscopic scale. The readers are referred to Ref. [2] for more details of the experimental testing procedure and result interpretation. These data are given in Tables 3, 5, 7 and 9. Note that in these tables, a range of the obtained Young's moduli are reported, in which the first value refer to the nanoindentation micro-measurements results and the second one to the macroscopic scale by extrapolating to zero porosity. Bearing in mind that in the experimental work, the Possion's ratio could not be determined directly, but an assumed value. The corresponding bulk and shear moduli, K and G are also provided, using the following equation with an assumed Poisson's ratio of 0.3:

$$K = \frac{E}{3(1 - 2v)}, \quad G = \frac{E}{2(1 + v)} \qquad (6)$$

The experimental results by Acker [42], who used the nanoindentation techniques to characterize the elastic properties of C_2S, C_3S and C_3A, are also reported. As seen, the results obtained by Acker are in a good agreement with the results by Velez et al. [2]. More recently, Moon et al. [43] used the high-pressure X-ray diffraction experiments to characterize the bulk moduli of the Tricalcium Aluminate C_3A. The bulk moduli of 102 GPa and 110 GPa were respectively obtained by fitting second- and third order finite

strain equation of state and are provided in Table 7. The other modulus were calculated based on the value of Poisson's ratio of 0.28 from their own DFT calculations [43].

Table 2 summarized all calculated elastic constants C_{ij} of C_2S. We can see that the values of C_{11}, C_{22} and C_{33} are comparable with each other and are in the range of 174–196 GPa. The material is expected to be less compressive in the second direction given the higher value of C_{22} compared to those of the C_{11} and C_{33}. The C_2S material is also expected to have a high shear resistance along the first direction, with a highest shear modulus C_{44} in comparison to C_{55} and C_{66}. Since C_2S is not a highly anisotropic material, a similarity in the directional elastic moduli plot can be observed in Fig. 2.

The isotropic bulk modulus and shear modulus of the phase C_2S were calculated according to the average VRH approximation as previously mentioned and the resulting DFT results are presented in Table 3, together with experimental data and force field calculations results for comparison. It can be seen that for this investigated C_2S phase, only IFF of the force-field methods yields a good estimation mechanic properties when comparing with DFT and experimental force field. The experimental value for Young modulus E was found in the range of 130–140 GPa, which is close to the predicted values by DFT-PBE-D2 and IFF simulations (131 GPa and 153 GPa, respectively). The Dreiding, universal and CVFF forcefields underestimated the bulk modulus by 100%, while other forcefields such as COMPASS, COMPASS II and clayFF overestimated the value around 50%.

It is also to see that the predicted mechanical properties by DFT-LDA method are higher than that of DFT-PBE-D2. While the difference in predicted lattice constants by the two methods was negligle, the corresponding simulations results would make the difference in the bulk modulus up to 30%. The DFT-LDA approach moderately overestimates all C_2S mechanical properties compared with experimental tests.

Table 4 presents all calculated elastic constants C_{ij} of C3S. We can see that the elastic moduli of C_3S are similar to those of C_2S values. However, unlike C_2S which is less compressive in the second direction, the Alite phase is expected to be less compressive in a

Table 2
Calculated elastic constants C_{ij} (GPa) of C2S. See Eq. 1 for more details on the direction of i,j notation.

C_{ij}	1	2	3	4	5	6
1	187.6	57.5	69.0	0.0	−5.2	0.0
2	57.5	195.8	44.3	0.0	0.8	0.0
3	69.0	44.3	174.0	0.0	−13.8	0.0
4	0.0	0.0	0.0	55.6	0.0	3.3
5	−5.2	0.8	−13.8	0.0	33.4	0.0
6	0.0	0.0	0.0	3.3	0.0	47.4

Table 3
Mechanical properties of C_2S.

Force field type	K (GPa)	E (GPa)	G (GPa)	v
COMPASS FF [11]	141	192	75	0.27
COMPASSII FF [11]	96	78	29	0.36
ClayFF [11]	165	221	87	0.27
Dreiding [11]	46	65	26	0.26
Universal [11]	44	62	25	0.26
CVFF [11]	53	69	27	0.28
INTERFACE [11]	103	153	61	0.25
Exp. [2]	108–117[a]	130–140	50–54[a]	0.3[b]
Exp. [42]	117 [a]	140	54[a]	0.3[b]
DFT-LDA (This work)	121	166	65	0.27
DFT-PBE-D2 (This work)	99	131	51	0.28

[a] derived values from Eqs. 6.
[b] assumed value of Poisson ratio.

Table 4

Calculated elastic constants C_{ij} (GPa) of C_3S. See Eq. 1 for more details on the direction of i,j notation.

C_{ij}	1	2	3	4	5	6
1	174.4	59.2	62.5	0.2	−2.4	−9.0
2	59.2	179.7	76.6	−6.9	−0.7	−2.5
3	62.5	76.6	201.6	1.3	−1.2	−10.2
4	0.2	−6.9	1.3	62.4	0.0	−0.7
5	−2.4	−0.7	−1.2	0.0	47.0	2.3
6	−9.0	−2.5	−10.2	−0.7	2.3	54.0

Table 5

Mechanical properties of C_3S.

Force field type	K (GPa)	E (GPa)	G (GPa)	v
COMPASSII FF [11]	130	113	42	0.35
Dreiding [11]	25	40	16	0.23
Universal [11]	28	42	17	0.25
CVFF [11]	35	51	20	0.26
INTERFACE [11]	104	162	65	0.24
INTERFACE [16]	104	144	56	0.27
DFT-PBE [27]	103	143	57	0.27
Exp. [2]	112–122[a]	135–147	52–56[a]	0.3[b]
Exp. [42]	112[a]	135	52[a]	0.3[b]
DFT-PBE-D2 (This work)	105	142	56	0.27

[a] derived values from Eqs. 6.
[b] assumed value of Poisson ratio.

Table 6

Calculated elastic constants C_{ij} (GPa) of C_3A. See Eq. 1 for more details on the direction of i,j notation.

C_{ij}	1	2	3	4	5	6
1	176.1	83.0	83.0	0.0	0.0	0.0
2	83.0	176.1	83.0	0.0	0.0	0.0
3	83.0	83.0	176.1	0.0	0.0	0.0
4	0.0	0.0	0.0	60.3	0.0	0.0
5	0.0	0.0	0.0	0.0	60.3	0.0
6	0.0	0.0	0.0	0.0	0.0	60.3

Table 7

Mechanical properties of C_3A.

Force field type	K (GPa)	E (GPa)	G (GPa)	v
COMPASSII FF [11]	34	48	19	0.27
ClayFF [11]	190	208	79	0.317
Dreiding [11]	54	77	30	0.26
Universal [11]	51	66	26	0.28
CVFF [11]	70	73	28	0.3
INTERFACE [11]	97	160	65	0.22
Exp. [2]	121–133[a]	145–160	58–61[a]	0.3[b]
Exp. [42]	133[a]	160	61[a]	0.3[b]
Exp. [43]	102–110	135–145[a]	53–57[a]	0.28[b]
DFT-PBE [43]	102	134	52	0.28
DFT-PBE [6]	103	139	54	0.28
DFT-PBE [44]	99	130	51	0.25
DFT-PBE-D2 (This work)	114	141	54	0.29

[a] derived values from Eqs. 6.
[b] assumed value of Poisson ratio.

Table 8

Calculated elastic constants C_{ij} (GPa) of C_4AF. See Eq. 1 for more details on the direction of i,j notation.

C_{ij}	1	2	3	4	5	6
1	218.0	109.5	56.0	0.0	0.0	1.9
2	109.5	174.5	90.7	0.0	0.0	−1.4
3	56.0	90.7	220.3	0.0	0.0	0.4
4	0.0	0.0	0.0	70.9	−0.2	0.0
5	0.0	0.0	0.0	−0.2	51.6	0.0
6	1.9	−1.4	0.4	0.0	0.0	73.7
6	0.0	0.0	0.0	0.0	0.0	81.0

Table 9
Mechanical properties of C_4AF.

Force field type	K (GPa)	E (GPa)	G (GPa)	v
ClayFF [11]	163	205	79	0.29
Dreiding [11]	224	288	112	0.28
Universal [11]	210	229	87	0.31
Exp. [2]	104[a]	125	48[a]	0.3 [b]
DFT-PBE-D2 (this work)	153	177	68	0.30
DFT-PBE-D2 spin-polarized (this work)	125	156	61	0.29

[a] derived values from Eqs. 6.
[b] assumed value of Poisson ratio.

third direction with a higher value of C_{33} in comparison to those of the C_{11} and C_{22}. In contrary, the C_3S is expected to exhibit the similar behaviour in shear as for C2S, with a higher shear resistance along the first direction. This is depicted by a more pronounced value of C_{44} than C_{55} and C_{66}. In addition, C_3S also represents a slightly anisotropic properties as can be seen from Fig. 3 showing a similarity in the directional elastic moduli.

The experimental and numerical elastic properties of C_3S evaluated using the RVH method are summarized in Table 5. It can be seen that the Young modulus E = 142 GPa calculated by our DFF simulations is within the experimental data range (135–147 GPa). The Bulk modulus K calculated by DFT was about 105 GPa, which is moderately lower than the experimental result (112–122 GPa). This is because our DFT simulation predicted a Poisson's ratio equal to 0.27, while an assumed value of 0.30 was used to calculate the experimental Bulk modulus. The mechanical properties predicted from classical force field methods were also documented in Table 5 for comparison. Again, the IFF force field
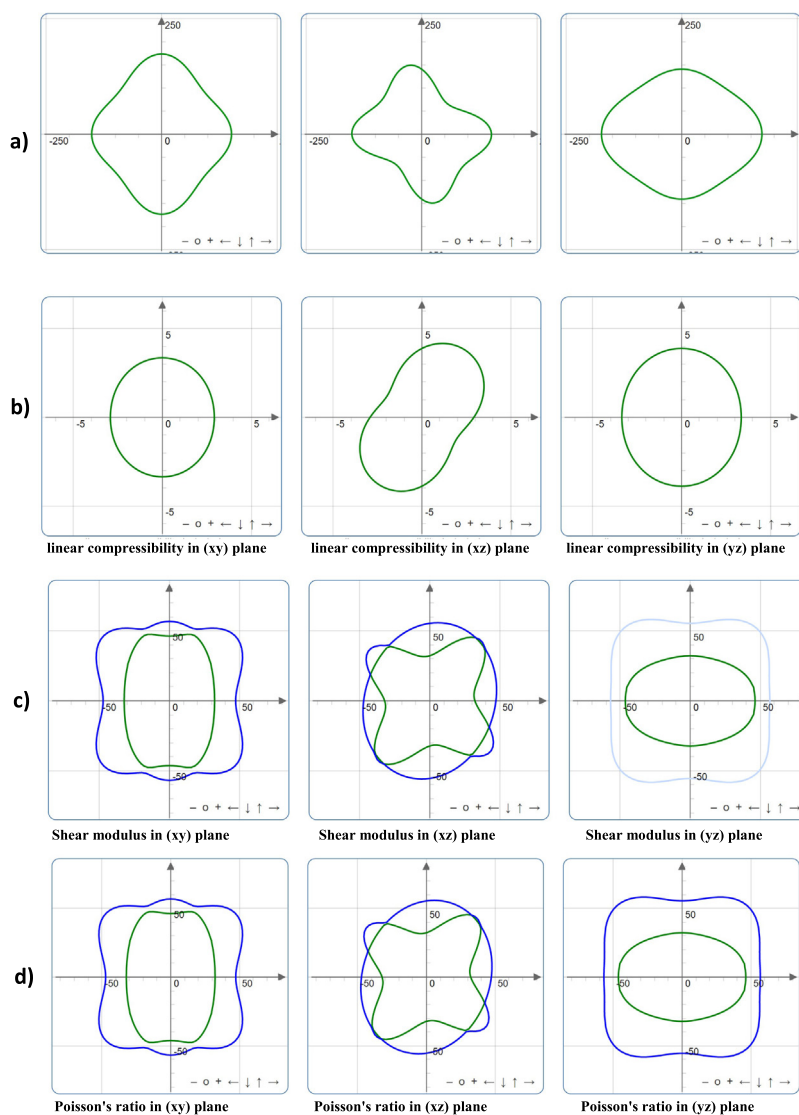

linear compressibility in (xy) plane   linear compressibility in (xz) plane   linear compressibility in (yz) plane

Shear modulus in (xy) plane   Shear modulus in (xz) plane   Shear modulus in (yz) plane

Poisson's ratio in (xy) plane   Poisson's ratio in (xz) plane   Poisson's ratio in (yz) plane

Fig. 2. Spatial dependence of (a) Young's modulus, (b) linear compressibility, (c) shear modulus, and (d) Poisson's ratio of C_2S.
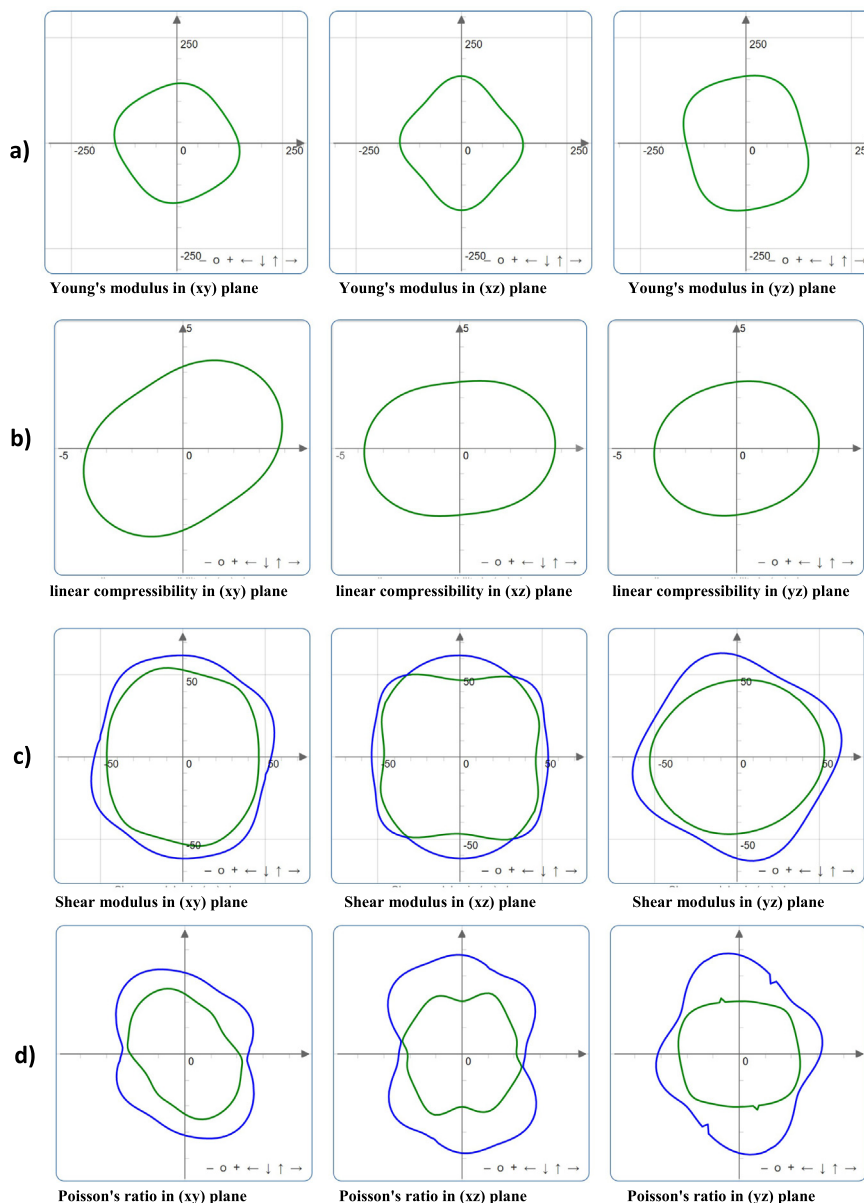
Fig. 3. Spatial dependence of (a) Young's modulus, (b) linear compressibility, (c) shear modulus, and (d) Poisson's ratio of C3S.

method gave the best predicted results in comparison with the experimental ones and DFT results. The resulting Young modulus E and shear modulus G obtained with the IFF method are just slightly overestimated with respect to the experiments. Other force fields methods (Dreiding, Universall, CVFF) underestimate significantly the experimental mechanical properties of C_3S. Furthermore, we see that our DFT-PBE-D2 results are consistent with the recent DFT-PBE work on C_3S by Laanaiya et al. [27]. This suggests the VdW correction effect is not substantial for the C_3S phase.

Table 6 reveal all calculated elastic constants C_{ij} of the C_3A phase. We can see that the predicted C_{11}, C_{22} and C_{33} are precisely the same and equal to 176 GPa, while the shear constants C_{44}, C_{55}, C_{66} are all equal to 60 GPa. This result demonstrates that the C_3A phase is isotropic. The isotropy in elastic behaviour of this clinker phase is also confirmed in Fig. 4 showing the same plots of the calculated directional elastic moduli. In Table 7, the resulting mechanical properties based on the RVH approximation are given. It can be seen that our DFT-PBE-D2 results are in good agreement with previous DFT-PBE calculations [43,45,44] and the experi-

ments. The VdW correction in the DFT calculations (PBE-D2) can yield to the increasing of maximum 10% of the K, E, G values compared with DFT-PBE methods. The calculated Young moduli E are in the same range of experimental data. The obtained results confirms the capability of the established DFT model with PBE-D2 method to reproduce the experimental mechanical behaviour of C3A. For comparison, the mechanical properties obtained with classical force field simulations have also been reported in Table 7. The IFF force field is, again, the best force field method to predict the elastic properties of C_3A. However, for this phase the IFF simulation underestimates the K value by 20%, overestimates the E and G moduli by 10%, as reported by Tavakoli et al.[11]. Other classical force fields either significantly undershoot or substantially overestimate the experimental K, G, E results of C_3A.

We have learned in the previous section that it is critical to include spin-polarization in the established DFT models for crystal lattice optimization. The identical effect was discovered for the elastic properties of C4AF structure. Table 8 presents all elastic constants C_{ij} of C_4AF calculated with spin-polarized DFT simulation.
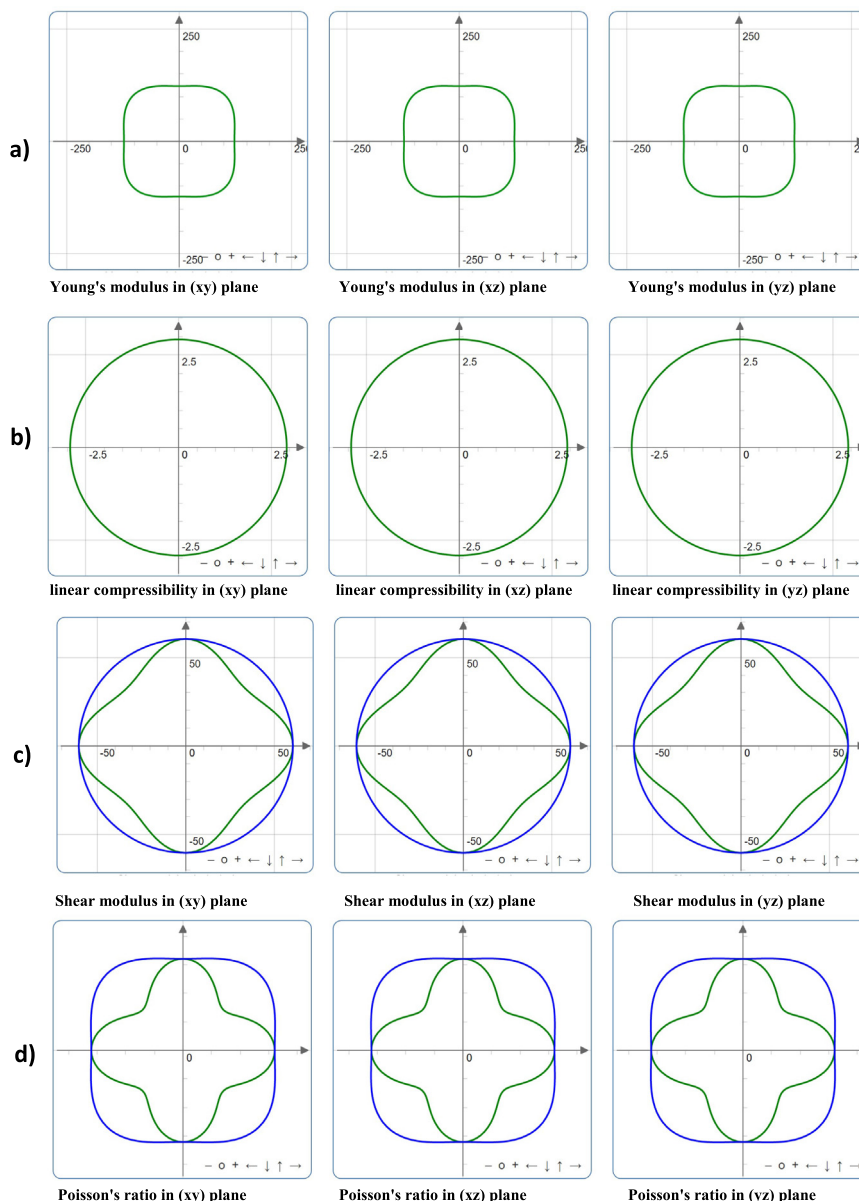
Fig. 4. Spatial dependence of (a) Young's modulus, (b) linear compressibility, (c) shear modulus, and (d) Poisson's ratio of C_3A.

The results show that the values of C_{11} and C_{33} are higher than C_{22}. Those values are in the range of 174–220 GPa. For shear elastic constants, the C_4AF phase has the lowest value in the second direction. The result implies that C_4AF is slightly anisotropic material. Note that there are several negative values of the non-orthogonal constants C_{ij} in the calculated elastic matrix. However, these values are small, and might come from the artifact of numerical calculations. More details on the directional elastic moduli are presented in Fig. 5. The resulting elastic properties calculated using the RVH method are reported in Table 9, along with experimental results and other force field model results which were investigated by Tavakoli et al. [11]. As seen, all of the investigated classical force field methods overestimated significantly other elastic moduli of the C_4AF phase. For example, the best force field method like ClayFF predicted a much higher value of Bulk modules with 60% in difference in comparison with experimental result. Our non-spin DFT prediction is also 50% off the experiment. When spin-polarization is included in the DFT calculation, the obtained results are significantly improved but still higher than the experimental

value with 25% in difference. This clearly shows that there is still a lot of room for improvement for both DFT and classical force field to obtain an adequate description of the ferrite phase.

3.3. Electronic properties

To investigate the electronic structure of C_2S, the contribution of each atom type (Calcium, Silicone, and Oxygen) to the total density of state(DOS) was determined. The energy of the Fermi level was relatively set to zero in all calculations. From Fig. 6, we see that both Oxygen and Calcium atoms contribute to the valence region; while the conductive region is dominated by Calcium atoms with a low contribution from Oxygen. Si atoms make a very small contribution to the total DOS. Our calculated band-gap of C_2S is 4.7 eV. This finding is in good agreement with the value of 5.3 eV calculated by Durgun et al. [23]. C_3S is composed of the same chemical elements as C_2S with Ca, Si and O atoms. However, the ratio of CaO: SiO_2 is higher than that of C_2S. The calculated DOS profile of C_3S is similar to that of C_2S, see Fig. 7. The contribution of each atom type
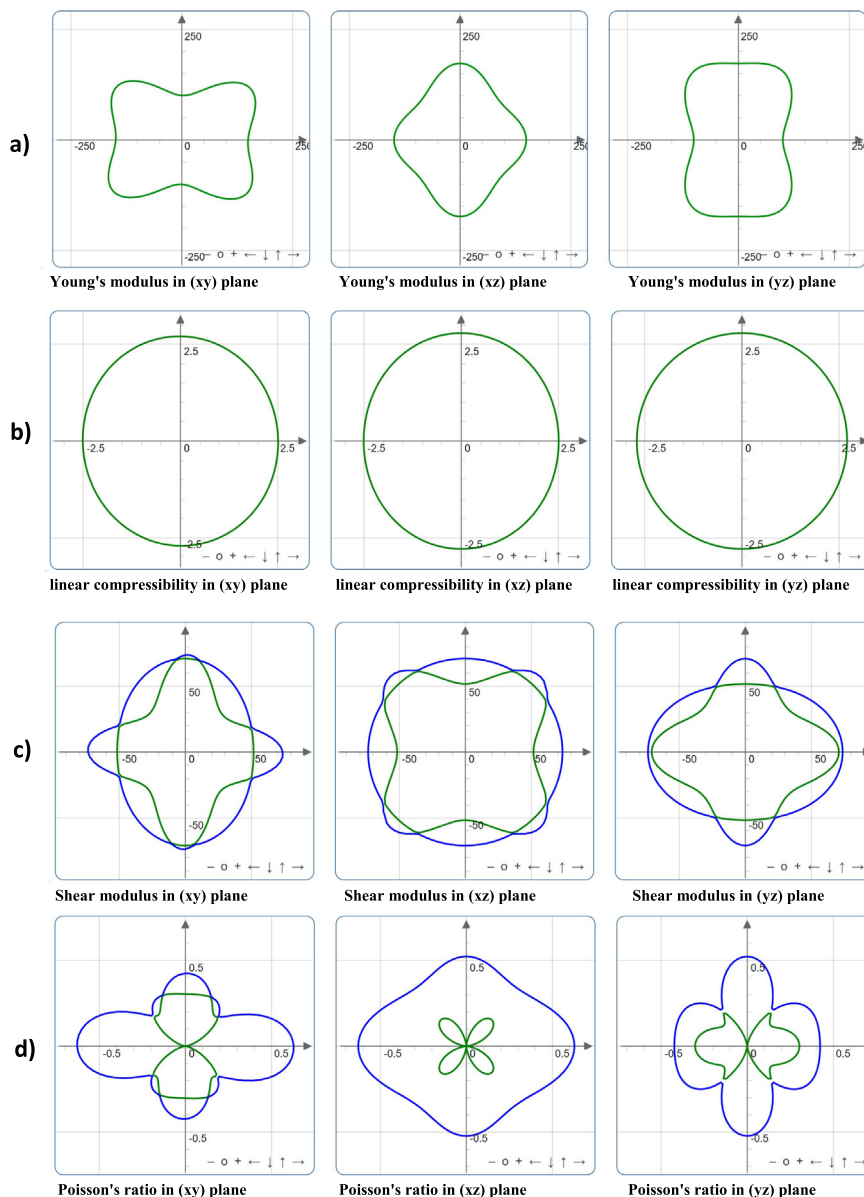
Fig. 5. Spatial dependence of (a) Young's modulus, (b) linear compressibility, (c) shear modulus, and (d) Poisson's ratio of C_4AF.
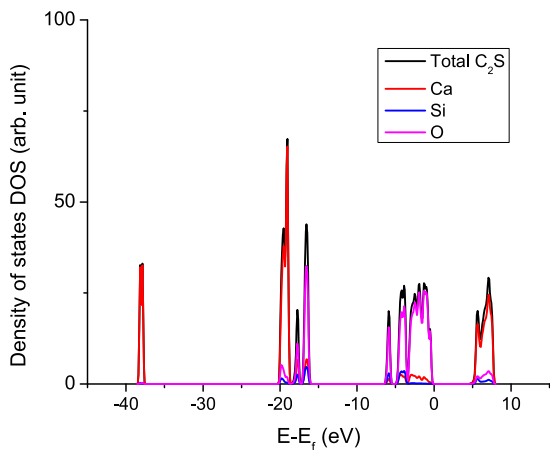

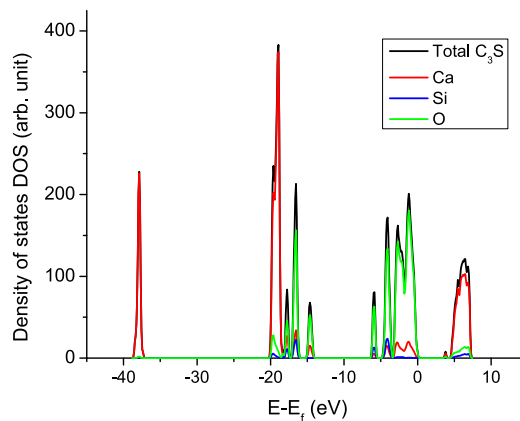**Fig. 6.** Total Density of State of C_2S with atomic contributions.

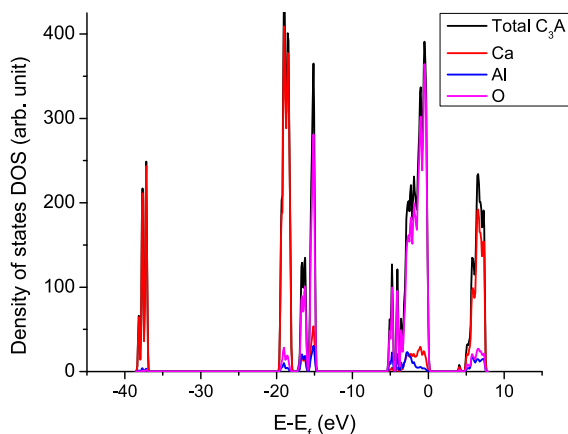**Fig. 7.** Total Density of State of C_3S with atomic contributions.

Fig. 8. Total Density of State of C_3A with atomic contributions.

to the total DOS shows the lowest impact of Si atom. The band-gap of C_3S from our simulation was found as 3.4 eV. This value is similar with the previous DFT calculations (3.57 eV [27] and 4.1 eV [23])

Fig. 8 shows the calculated DOS of C_3A structure. We can observe that again Ca and O dominate the valence region. There is a minor contribution from Al atom. This is mainly because Al_2O_3 constitutes only 25% of the chemical composition of C_3A; while CaO contributes 75% to the chemical composition. However, it is interesting to know that the band-gap energy of C_3A (3.6 eV) is very close to that of C_3S (3.4 eV). Thus, we can conclude the effect of SiO_2 or Al_2O_3 is similar to the total DOS in C_3S and C_3A materials. The calculated DOS of C_4AF with both spin-up and spin-down are shown in Fig. 9.

To get more insight into the charge of various atoms, the Löwdin charge calculation was performed with Quantum Espresso software for all crystal structures. The average of the atomic charge of each atom type is presented in Table 10. The atomic charge obtained by other method such as Bader charge, charge from classical IFF force field and equivalent charges obtained from experiment were added for comparison. For C_2S structure, the atomic charge for Ca, Si, and O are 0.88e, 1.61e, and −0.77e, respectively. It is quite interesting that the Löwdin method significantly underestimates the Ca^{2+} ion in C_2S structure. The charge of +1.5e for Ca^{2+} from Bader charge and IFF are more consistent with each others and are closer to the formal charge +2e. However, the Bader model
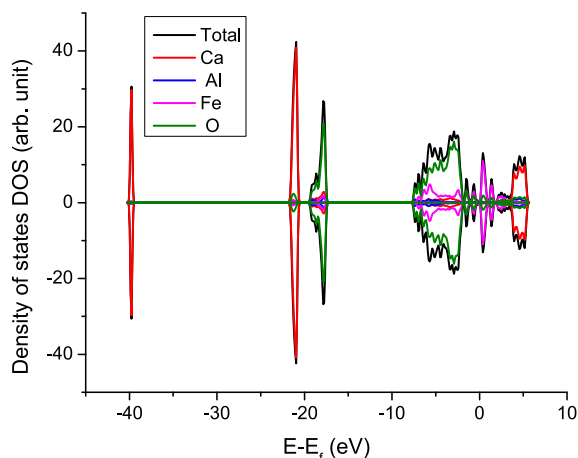

Fig. 9. Total Density of State of C_4AF with atomic contributions. The DOS from both spin-up and spin-down calculations are shown.

shows an overshoot for the charge of Silicon atom (+3.6e). While the experiments [46] and IFF yields a reasonable Si charge (+1.0e), the Löwdin charge is calculated as +1.6e. So the IFF charge is closest with the experimental one for Si atom. From the oxygen atom, the Bader model predicted as −1.53e, which is a higher than the Löwdin charge (−0.77e) and experimental one (−0.6e). The charge of C_3S and C_2S for all atoms are comparable. The charge of atoms Ca and Si are only 0.02e higher in C_2S.

For C_3A structure, there is no Si atom but Al atom instead. In that manner, The Löwdin charge predicts that the atomic charge of Ca atom in C_3A is more moderate than in C_3S; while the charge of Al (1.19 e) in C_3A is less than that of Si in C_3S (1.63 e). As a result, the negative charge of oxygen atom is higher in C_3A than in C_3S material. In addition, we can see that the Löwdin charge, IFF charge for Aluminum and Oxygen atoms are very close to the experimental value of Al_2O_3 phase [46,47]. Moreover, the data show very interesting results for the atomic charge of C_4AF phase. The charge of Ca and Al are similar to that of C_3A. However, the lowest charge is located at the Fe metal atom. As a result, the average oxygen atoms in C_4AF are also less negative charged than in other phases (C_2S, C_3S, C_3A). This indicates that the effect of Fe to the atomic charge of all other atoms in C_4AF is significant. However, we need to underline that there is a limitation for the QM-derived charge which was discussed in literature [48–50]. Therefore, taking directly the QM-charge into the classical force field might cause unreasonable results. It is important to note that there are several methods to calculate the QM-charge as documented by, e.g. Mulliken [51], Bader [52], Hirshfeld [53], Löwdin [31]. To select a good charge model is challenging and often system dependant, the readers are referred to [54,55] for a more insight of the charge models.

3.4. Thermodynamic properties

The thermodynamics property at different temperature range is among the interesting properties of these phases in the context of high temperature application. Several important parameters such as the free energy, entropy and heat capacity were calculated by DFT-PBE-D2 method and presented her. We limited in a temperature range from 0 K-800 K for those calculation. One small note is that in the DFT calculation, the heat capacity at constant volume C_v was calculated. However the C_v value is almost the same as the heat capacity at constant pressure C_p for solid structure. Therefore, we can directly compare our calculated C_v with the experimental C_p value. The results for the calcium silicate phase C_2S and C_3S are depicted in Fig. 10. It is common to observe that free energy decreases over temperature, while entropy and thermal capacity increase. The C_2S and C_3S pattern is very similar but the value of certain C_3S properties is higher than that of C_2S. This is because the number of atoms per mol of C_3S is higher than that of C_2S, therefore the entropy and the heat capacity is expected to be greater than shown in Fig. 10.

The experimental value of the heat capacity of C_2S and C_3S was collected at T = 298 K and compared with the calculated values. Our DFT-PBE-D2 method yielded the values of 125 J/mol/K and 186 J/mol/K for the heat capacity of C_2S and C_3S, respectively. These values are in a good agreement with experimental value within 10% (See Table 11).

Fig. 11 presented the calculated thermodynamic properties of phases C_3A and C_4AF. The increase in entropy value in these materials is higher than in C_2S and C_3S. The same trend is observed for the value of C_v. This is not surprising because C_3A and C_4AF have more atoms per mole than C_2S, C_3S phase. We also compare the calculated C_v with the value of the experiments. The calculated C_v of C_3A is within 10% of the experimental value error. However, the ferrite phase C_4AF again shows a large deviation. The DFT-PBE-

Table 10
Calculated atomic charge (electron) of different atom type in the main phases.

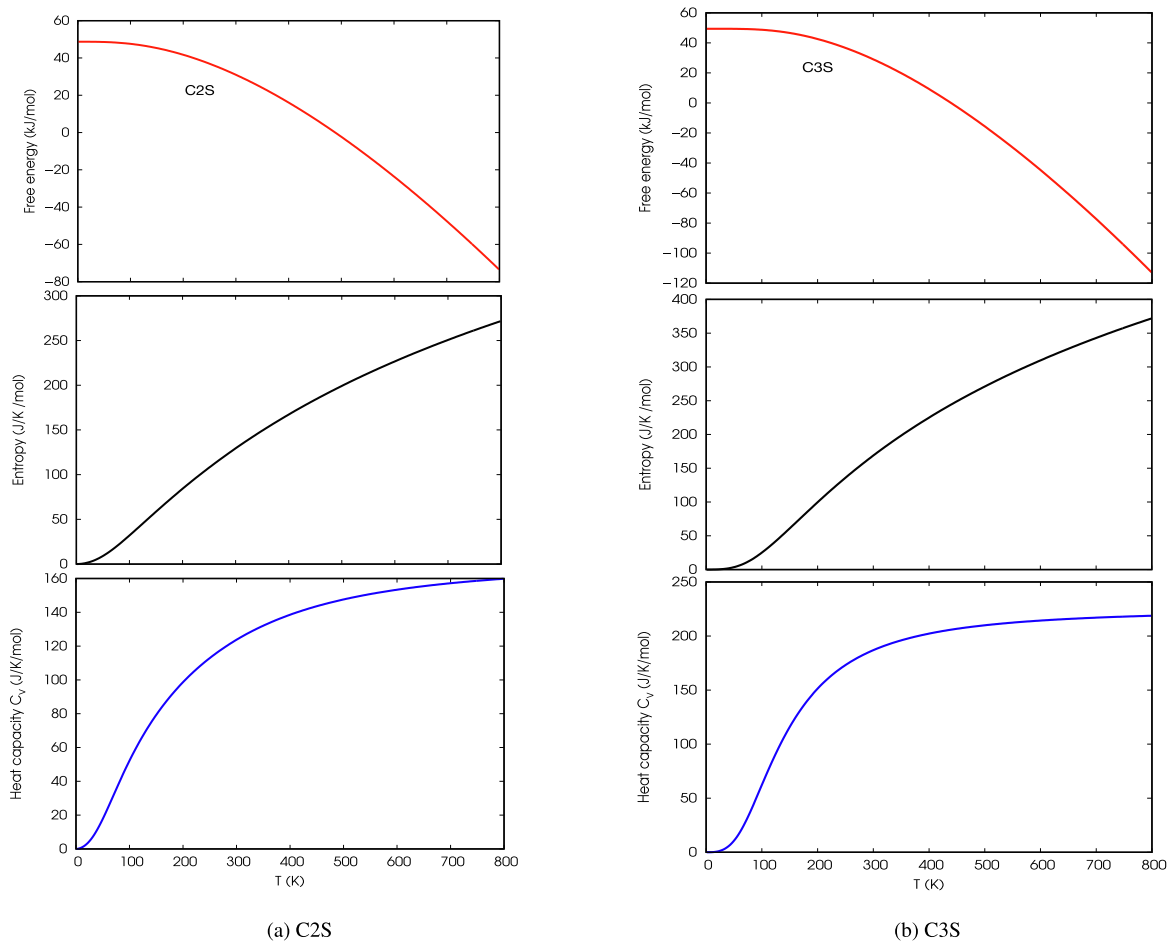| Atom	Charge method	C_2S	C_3S	C_3A	C_4AF
Ca	Löwdin (this work)	+0.88	+0.86	+0.92	+0.94
	Bader [23,27]	+1.53	+1.53	/	/
	IFF [16]	+1.5	+1.5	+1.5	+1.5
Si	Löwdin (this work)	+1.61	+1.63	/	/
	Bader [23,27]	+3.08	+3.05	/	/
	IFF [16]	+1.0	+1.0	/	/
	Exp. [46,27]	+1.0	+1.0	/	/
Al	Löwdin (this work)	/	/	+1.19	+1.19
	IFF [16]	/	/	+1.2	/
	Exp. [46,47]	/	/	+1.4, +1.32	+1.4, +1.32
Fe	Löwdin (this work)	/	/	/	+0.47
O	Löwdin (this work)	−0.77	−0.77	−0.80	−0.66
	Bader [23,27]	−1.53	−1.44 − 1.55	/	/
	IFF [16]	−1.0 − −1.5	−1.0 − −1.5	/	/
	Exp. [46,47]	−0.6	−0.6	−0.6, −0.88	−0.6, −0.88

(a) C2S   (b) C3S

Fig. 10. Calculated thermodynamic properties (free energy, entropy and heat capacity) of C_2S and C_3S phases for the temperature range of 0 K – 800 K.

Table 11
Heat capacity (J/mol/K) of different phases at 298 K. Experimental values are taken from [56] for comparison.

Phases	Heat capacity Exp.	Calculated Heat capacity DFT-PBE-D2(this work)	Relative error (%)
C_2S	129	125	−3
C_3S	172	186	8
C_3A	210	228	9
C_4AF	396	286	−28

D2 method underestimates the heat capacity of C_4AF by almost 30%.

3.5. Discussions

It is very important to note that the porosity has a strong effect on the microscopic elastic properties in the real experimental testing. The work of Velez et al.[2] claimed that the mechanical strength of the four clinker phases decreased with increasing porosity with nano-indentation techniques. This is due to the void
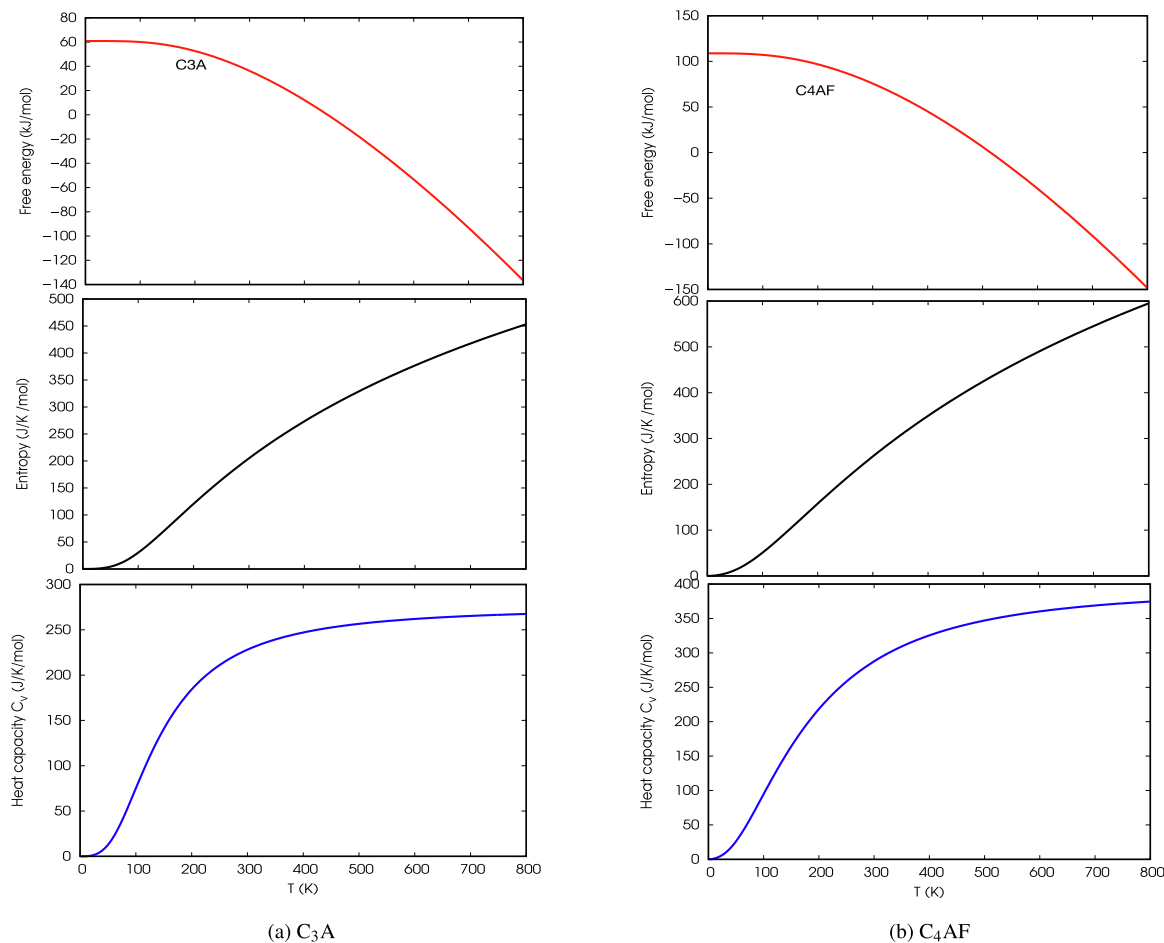
Fig. 11. Calculated thermodynamic properties (free energy, entropy and heat capacity) of C_3A and C_4AF phases for the temperature range of 0 K – 800 K.

pores between the particles but not to the porosity of the particles themselves. Therefore, the extrapolated value at zero porosity corresponds to the perfect crystal structure. In our DFT simulation, the model was the perfect crystalline structure of the clinker phases without porosity. It is very desirable to include the effect of porosity in the atomistic simulations. This would, however, significantly increase the number of atoms in the system and could be too expensive for DFT methods to perform. An alternative approach, such as molecular dynamics or a continuum model, would therefore be more suitable in this situation.

The novelty of this work is the systematic investigations on electronic and thermodynamic properties of the four main phases of Portland cement. The new inside of the ferrite structure C_4AF has marked an important message for the computational community of the cement modeling. The findings suggest the significance of the magnetic moment of the Fe atom. This is worth further effort to strengthen the description of both structural and mechanical properties.

The calculated data from this work can partially be associated with the reactivity of the clinker phases. For example, the physical chemistry of the phases can be explored by the atomic charge obtained from this DFT study. The simulated density of states given by this work may also help to understand the chemical bonding properties of the phases. However, further studies are required to a better understanding of the reactions in the environment between cement phases and various chemicals.

One of the ultimate goals is to understand the connection between the overall characteristics of Portland cement and the

property of the four main phases. To archive this objective, there are several important variables to be considered, such as phase mass fraction, porosity, microscopic phase structure, etc. The role of hydrated structure and minor phases is also essential for the overall properties. This is more significant when Portland cement is used as a binding material in concrete because of its dynamic environment. The knowledge of the dynamic mechanism at the molecular level is critical for the development of building and construction materials. Therefore, this study provides ab initio data of mechanical and thermodynamic properties at nanoscale. Using these results as inputs for larger and more complex modeling, to incorporate more structural parameters such as porosity, reaction with water, particle size, etc., to advance the field of cement modeling.

4. Conclusions

The present work investigated the capability of ab initio atomistic simulations using DFT method with PBE-D2 functional to predict the mechanical and lattice properties of four major phases of Portland clinker. These results led to the following conclusions:

- The obtained results in terms mechanical properties and lattice constants by the established DFT models were in excellent agreement with the experiments data for the three structures (C_2S, C_3S, and C_3A). However for C_4AF phase, the established model still overshoot the experimental mechanical properties, even though the lattice constants were predicted reasonably.

- It is interesting to note that the inclusion of VdW interactions in the DFT calculation was not as significant as spin-polarized treatment for the C_4AF structure. Calculated mechanical modules, including spin-polarization, are the best theoretical value to date, but are still overestimated by about 20% compared to previous studies.
- The present study also expanded existing knowledge of the mechanical, electronic and thermodynamic properties of the four main phases of the Portland cement clinker. The predicted spatial dependence of the elastic properties means that all phases are either isotropic or slightly anisotropic. This work has produced more clear results on the electronic and thermodynamic properties that are critical for validating the existing models, thereby increasing their reliability and robustness in the design of the material.
- The results of the DFT simulation offered a supplement to the classical force fields used to model the four clinker phases. For example, the IFF force field could provide a fair explanation of the properties of C_2S, C_3S and C_3A materials. To the authors' knowledge, the simulation of the C_4AF phase of ferrite using the classical force field was limited in literature. Notice that the computational cost of DFT is far higher than that of FFs, and therefore ab initio atomistic simulations can be used on a local scale as necessary.
- Finally, along with the latest advance in force-fields and continuum-scale simulations, the cement community will have complementary multi-scale computational tools to bridge the understanding of cement materials at a broader time and duration, and to advance cement research in the near future. Further research is still required to improve the existing DFT models to predict the mechanical properties of the Porland clinker ferrite phase and to optimize the associated computational times. Considering, for example, spin–orbit coupling, DFT + U (Hubbard) correction, more functional DFTs such as hybrid or double hybrid methods may be a possibility for future studies. Thus, the current simulation results have been very promising to show the possibility of using only one DFT framework to model the four cement clinker phases.

CRediT authorship contribution statement

Ngoc Lan Mai: Writing - original draft, Methodology, Software, Investigation. **Nguyen Hieu Hoang:** Investigation, Validation, Writing - original draft, Writing - review & editing, Funding acquisition. **Ha T. Do:** Investigation, Validation, Writing - review & editing. **Monika Pilz:** Investigation, Validation, Writing - review & editing. **Thuat T. Trinh:** Conceptualization, Validation, Supervision, Resources, Writing - review & editing.

Declaration of Competing Interest

The authors declare that they have no known competing financial interests or personal relationships that could have appeared to influence the work reported in this paper.

Acknowledgments

References

[1] H. Taylor, Cement Chemistry, vol. 2, Thomas Telford Publishing, 1997. doi:10.1680/cc.25929. URL:https://doi.org/10.1680/cc.25929..

[2] K. Velez, S. Maximilien, D. Damidot, G. Fantozzi, F. Sorrentino, Determination by nanoindentation of elastic modulus and hardness of pure constituents of Portland cement clinker, Cem. Concr. Res. 31 (4) (2001) 555–561, https://doi.org/10.1016/s0008-8846(00)00505-6.

[3] A. Boumiz, D. Sorrentino, C. Vernet, F. Tenoudji, Modelling the development of the elastic moduli as a function of the hydration degree of cement pastes and mortars, Proceedings of the 2nd RILEM Workshop on Hydration and Setting: Why Does Cement Set? An Interdisciplinary Approach (1997) 295–316..

[4] M. Sebastiani, R. Moscatelli, F. Ridi, P. Baglioni, F. Carassiti, High-resolution high-speed nanoindentation mapping of cement pastes: Unravelling the effect of microstructure on the mechanical properties of hydrated phases, Mater. Design 97 (2016) 372–380, https://doi.org/10.1016/j.matdes.2016.02.087. URL:http://www.sciencedirect.com/science/article/pii/S0264127516302362.

[5] H. Manzano, E. Durgun, M.J. Abdolhosseine Qomi, F.-J. Ulm, R. Pellenq, J. Grossman, Impact of chemical impurities on the crystalline cement clinker phases determined by atomistic simulations, Cryst. Growth Des. 11 (7) (2011) 2964–2972, https://doi.org/10.1021/cg200212c.

[6] H. Manzano, J.S. Dolado, A. Ayuela, Structural, mechanical, and reactivity properties of tricalcium aluminate using first-principles calculations, J. Am. Ceram. Soc. 92 (4) (2009) 897–902, https://doi.org/10.1111/j.1551-2916.2009.02963.x.

[7] H. Manzano, J. Dolado, A. Ayuela, Elastic properties of the main species present in Portland cement pastes, Acta Mater. 57 (5) (2009) 1666–1674, https://doi.org/10.1016/j.actamat.2008.12.007.

[8] H. Manzano, E. Durgun, I. López-Arbeloa, J.C. Grossman, Insight on tricalcium silicate hydration and dissolution mechanism from molecular simulations, ACS Appl. Mater. Interfaces 7 (27) (2015) 14726–14733, https://doi.org/10.1021/acsami.5b02505.

[9] R.K. Mishra, L. Fernández-Carrasco, R.J. Flatt, H. Heinz, A force field for tricalcium aluminate to characterize surface properties, initial hydration, and organically modified interfaces in atomic resolution, Dalton Trans. 43 (27) (2014) 10602–10616, https://doi.org/10.1039/c4dt00438h.

[10] R.K. Mishra, L. Fernández-Carrasco, R.J. Flatt, H. Heinz, A force field for tricalcium aluminate to characterize surface properties, initial hydration, and organically modified interfaces in atomic resolution, Dalton Trans. 43 (27) (2014) 10602–10616, https://doi.org/10.1039/c4dt00438h.

[11] D. Tavakoli, A. Tarighat, Molecular dynamics study on the mechanical properties of Portland cement clinker phases, Comput. Mater. Sci. 119 (2016) 65–73, https://doi.org/10.1016/j.commatsci.2016.03.043.

[12] R.K. Mishra, A.K. Mohamed, D. Geissbühler, H. Manzano, T. Jamil, R. Shahsavari, A.G. Kalinichev, S. Galmarini, L. Tao, H. Heinz, R. Pellenq, A.C. van Duin, S.C. Parker, R.J. Flatt, P. Bowen, A force field database for cementitious materials including validations, applications and opportunities, Cem. Concr. Res. 102 (2017) 68–89, https://doi.org/10.1016/j.cemconres.2017.09.003.

[13] R.T. Cygan, J.-J. Liang, A.G. Kalinichev, Molecular models of hydroxide, oxyhydroxide, and clay phases and the development of a general force field, J. Phys. Chem. B 108 (4) (2004) 1255–1266, https://doi.org/10.1021/jp0363287.

[14] H. Heinz, T.-J. Lin, R. Kishore Mishra, F.S. Emami, Thermodynamically consistent force fields for the assembly of inorganic, organic, and biological nanostructures: The INTERFACE force field, Langmuir 29 (6) (2013) 1754–1765, https://doi.org/10.1021/la3038846.

[15] A.C. van Duin, S. Dasgupta, F. Lorant, W.A. Goddard, ReaxFF: a reactive force field for hydrocarbons, J. Phys. Chem. A 105 (41) (2001) 9396–9409, https://doi.org/10.1021/jp004368u.

[16] R.K. Mishra, R.J. Flatt, H. Heinz, Force field for tricalcium silicate and insight into nanoscale properties: cleavage, initial hydration, and adsorption of organic molecules, J. Phys. Chem. C 117 (20) (2013) 10417–10432.

[17] J.P. Perdew, K. Burke, M. Ernzerhof, Generalized gradient approximation made simple, Phys. Rev. Lett. 77 (18) (1996) 3865–3868, https://doi.org/10.1103/physrevlett.77.3865.

[18] R. Dovesi, B. Civalleri, R. Orlando, C. Roetti, V.R. Saunders, Ab initio quantum simulation in solid state chemistry, Rev. Comput. Chem. 21 (2005) 1.

[19] P.J. Hasnip, K. Refson, M.I. Probert, J.R. Yates, S.J. Clark, C.J. Pickard, Density functional theory in the solid state, Philosophical Transactions of the Royal Society A: Mathematical, Phys. Eng. Sci. 372 (2011) (2014) 20130270.

[20] J. Hafner, Ab-initio simulations of materials using vasp: Density-functional theory and beyond, J. Comput. Chem. 29 (13) (2008) 2044–2078.

[21] E. Pustovgar, R.K. Mishra, M. Palacios, J.-B. d. de Lacaillerie, T. Matschei, A.S. Andreev, H. Heinz, R. Verel, R.J. Flatt, Influence of aluminates on the hydration kinetics of tricalcium silicate, Cement and Concrete Research 100 (2017) 245–262..

[22] T. Jamil, A. Javadi, H. Heinz, Mechanism of molecular interaction of acrylate-polyethylene glycol acrylate copolymers with calcium silicate hydrate surfaces, Green Chem. 22 (5) (2020) 1577–1593.

[23] E. Durgun, H. Manzano, R. Pellenq, J.C. Grossman, Understanding and controlling the reactivity of the calcium silicate phases from first principles, Chem. Mater. 24 (7) (2012) 1262–1267, https://doi.org/10.1021/cm203127m.

[24] Q. Wang, H. Manzano, Y. Guo, I. Lopez-Arbeloa, X. Shen, Hydration mechanism of reactive and passive dicalcium silicate polymorphs from molecular

simulations, J. Phys. Chem. C 119 (34) (2015) 19869–19875, https://doi.org/10.1021/acs.jpcc.5b05257.

[25] I.-H. Svenum, I.G. Ringdalen, F.L. Bleken, J. Friis, D. Höche, O. Swang, Structure, hydration, and chloride ingress in c-s-h: Insight from DFT calculations, Cem. Concr. Res. 129 (2020), https://doi.org/10.1016/j.cemconres.2019.105965 105965.

[26] A. Kunhi Mohamed, S.C. Parker, P. Bowen, S. Galmarini, An atomistic building block description of c-s-h - towards a realistic c-s-h model, Cem. Concr. Res. 107 (2018) 221–235, https://doi.org/10.1016/j.cemconres.2018.01.007.

[27] M. Laanaiya, A. Bouibes, A. Zaoui, Understanding why alite is responsible of the main mechanical characteristics in Portland cement, Cem. Concr. Res. 126 (2019), https://doi.org/10.1016/j.cemconres.2019.105916 105916.

[28] K.F. Garrity, J.W. Bennett, K.M. Rabe, D. Vanderbilt, Pseudopotentials for high-throughput DFT calculations, Comput. Mater. Sci. 81 (2014) 446–452, https://doi.org/10.1016/j.commatsci.2013.08.053.

[29] P. Giannozzi, S. Baroni, N. Bonini, M. Calandra, R. Car, C. Cavazzoni, D. Ceresoli, G. L. Chiarotti, M. Cococcioni, I. Dabo, A. Dal Corso, S. de Gironcoli, S. Fabris, G. Fratesi, R. Gebauer, U. Gerstmann, C. Gougoussis, A. Kokalj, M. Lazzeri, L. Martin-Samos, N. Marzari, F. Mauri, R. Mazzarello, S. Paolini, A. Pasquarello, L. Paulatto, C. Sbraccia, S. Scandolo, G. Sclauzero, A.P. Seitsonen, A. Smogunov, P. Umari, R.M. Wentzcovitch, QUANTUM ESPRESSO: A modular and open-source software project for quantum simulations of materials, J. Phys.: Condens. Matter 21 (39) (2009), https://doi.org/10.1088/0953-8984/21/39/395502 395502.

[30] K. Momma, F. Izumi, Vesta 3 for three-dimensional visualization of crystal, volumetric and morphology data, J. Appl. Crystallography 44 (6) (2011) 1272–1276.

[31] P. Löwdin, On the non-orthogonality problem connected with the use of atomic wave functions in the theory of molecules and crystals, J. Chem. Phys. 18 (3) (1950) 365–375, https://doi.org/10.1063/1.1747632.

[32] G. te Velde, F. Bickelhaupt, E. Baerends, C. Fonseca Guerra, S. van Gisbergen, J. Snijders, T. Ziegler, Chemistry with ADF, J. Comput. Chem. 22 (9) (2001) 931–967. doi:10.1002/jcc.1056. URL:https://doi.org/10.1002/jcc.1056.

[33] S. Grimme, J. Antony, S. Ehrlich, H. Krieg, A consistent and accurate ab initio parametrization of density functional dispersion correction (DFT-d) for the 94 elements h-Pu, J. Chem. Phys. 132 (15) (2010), https://doi.org/10.1063/1.3382344 154104.

[34] A. Dal Corso, Elastic constants of beryllium: A first-principles investigation, J. Phys.: Condens. Matter 28 (7) (2016), https://doi.org/10.1088/0953-8984/28/7/075401 075401.

[35] R. Gaillac, P. Pullumbi, F.-X. Coudert, ELATE: An open-source online application for analysis and visualization of elastic tensors, J. Phys.: Condens. Matter 28 (27) (2016), https://doi.org/10.1088/0953-8984/28/27/275201 275201.

[36] M. Palumbo, A. Dal Corso, Lattice dynamics and thermophysical properties of hcp os and ru from the quasi-harmonic approximation, J. Phys.: Condens. Matter 29 (39) (2017) 395401.

[37] Y. Meng, X.-W. Liu, C.-F. Huo, W.-P. Guo, D.-B. Cao, Q. Peng, A. Dearden, X. Gonze, Y. Yang, J. Wang, H. Jiao, Y. Li, X.-D. Wen, When density functional approximations meet iron oxides, J. Chem. Theory Comput. 12 (10) (2016) 5132–5144, https://doi.org/10.1021/acs.jctc.6b00640.

[38] T. Tsurumi, Y. Hirano, H. Kato, T. Kamiya, M. Daimon, Crystal structure and hydration of belite, Ceram. Trans. 40 (1994) 19–25.

[39] G. De la Torre, R.N. De Vera, A.J. Cuberos, M. Aranda, Crystal structure of low magnesium-content alite: Application to rietveld quantitative phase analysis, Cem. Concr. Res. 38 (11) (2008) 1261–1269, https://doi.org/10.1016/j.cemconres.2008.06.005.

[40] P. Mondal, J. Jeffery, The crystal structure of tricalcium aluminate, Ca3Al2O6, Acta Crystallogr. Sect. B 31 (3) (1975) 689–697, https://doi.org/10.1107/s0567740875003639. URL:https://doi.org/10.1107/s0567740875003639.

[41] A. Colville, S. Geller, The crystal structure of brownmillerite, Ca2FeAlO5, Acta Crystallogr Sect B 27 (12) (1971) 2311–2315, https://doi.org/10.1107/s056774087100579x. URL:https://doi.org/10.1107/s056774087100579x.

[42] P. Acker, Micromechanical analysis of creep and shrinkage mechanisms. creep, shrinkage and durability mechanics of concrete and other quasi-brittle materials, Cambridge 264 (2001) 15–25.

[43] J. Moon, S. Yoon, R.M. Wentzcovitch, S.M. Clark, P.J. Monteiro, Elastic properties of tricalcium aluminate from high-pressure experiments and first-principles calculations, J. Am. Ceram. Soc. 95 (9) (2012) 2972–2978.

[44] C. Qi, D. Spagnoli, A. Fourie, Structural, electronic, and mechanical properties of calcium aluminate cements: Insight from first-principles theory, Constr. Build. Mater. 264 (2020) 120259.

[45] H. Manzano, Atomistic simulation studies of the cement paste components, Atomistic Simulation Studies of the Cement Paste Components (2009).

[46] N. Thong, D. Schwarzenbach, The use of electric field gradient calculations in charge density refinements. II. charge density refinement of the low-quartz structure of aluminum phosphate, Acta Cryst. Sect. A 35 (4) (1979) 658–664, https://doi.org/10.1107/s0567739479001522.

[47] J. Lewis, D. Schwarzenbach, H. Flack, Electric field gradients and charge density in corundum, α-Al$_2$O$_3$, Acta Cryst Sect A 38 (5) (1982) 733–739, https://doi.org/10.1107/s0567739482001478.

[48] K.C. Gross, P.G. Seybold, C.M. Hadad, Comparison of different atomic charge schemes for predicting pka variations in substituted anilines and phenols, Int. J. Quantum Chem. 90 (1) (2002) 445–458.

[49] B. Wang, S.L. Li, D.G. Truhlar, Modeling the partial atomic charges in inorganometallic molecules and solids and charge redistribution in lithium-ion cathodes, J. Chem. Theory Comput. 10 (12) (2014) 5640–5650.

[50] H. Heinz, U.W. Suter, Atomic charges for classical simulations of polar systems, J. Phys. Chem. B 108 (47) (2004) 18341–18352.

[51] R.S. Mulliken, Electronic population analysis on lcao–mo molecular wave functions. i, J. Chem. Phys. 23 (10) (1955) 1833–1840.

[52] R.F. Bader, A quantum theory of molecular structure and its applications, Chem. Rev. 91 (5) (1991) 893–928.

[53] F.L. Hirshfeld, Bonded-atom fragments for describing molecular charge densities, Theoretica chimica acta 44 (2) (1977) 129–138.

[54] D. Jacquemin, T. Le Bahers, C. Adamo, I. Ciofini, What is the "best" atomic charge model to describe through-space charge-transfer excitations?, PCCP 14 (16) (2012) 5383–5388.

[55] A.D. Laurent, D. Jacquemin, Td-dft benchmarks: a review, Int. J. Quantum Chem. 113 (17) (2013) 2019–2039.

[56] F. Lavergne, A.B. Fraj, I. Bayane, J. Barthélémy, Estimating the mechanical properties of hydrating blended cementitious materials: An investigation based on micromechanics, Cem. Concr. Res. 104 (2018) 37–60.